Breit-Wigner-Fano line shapes in Raman spectra of graphene

Eddwi H. Hasdeo,[1,*] Ahmad R. T. Nugraha,[1] Mildred S. Dresselhaus,[2,3] and Riichiro Saito[1]

[1]*Department of Physics, Tohoku University, Sendai 980-8578, Japan*
[2]*Department of Electrical Engineering and Computer Science, Massachusetts Institute of Technology,*
Cambridge, Massachusetts 02139-4037, USA
[3]*Department of Physics, Massachusetts Institute of Technology, Cambridge, Massachusetts 02139-4307, USA*

Excitation of electron-hole pairs in the vicinity of the Dirac cone by the Coulomb interaction gives rise to an asymmetric Breit-Wigner-Fano line shape in the phonon Raman spectra in graphene. This asymmetric line shape appears due to the interference effect between the phonon spectra and the electron-hole pair excitation spectra. The calculated Breit-Wigner-Fano asymmetric factor $1/q_{\mathrm{BWF}}$ as a function of the Fermi energy shows a V-shaped curve with a minimum value at the charge neutrality point and gives good agreement with the experimental results.

I. INTRODUCTION

Elementary excitations such as electrons and phonons can be probed by the inelastic scattering of light using the Raman spectroscopy technique. In graphene-related systems, studying the shape of the Raman spectra can give us a deep understanding of the electron energy dispersion [1], phonon energy dispersion [2], lifetime of excitations [3], the Kohn anomaly effect [4], and structure characterization [5]. In particular, the asymmetric Breit-Wigner-Fano (BWF) line shape, historically observed in the Raman spectra of graphite intercalation compounds (GICs) [6] and metallic nanotubes (m-SWNTs) [7], probes the interference between the continuum spectra with the discrete spectra [8]. Recently, the BWF asymmetry has been observed by Yoon *et al.* [9] in monolayer graphene indicating a common origin of the BWF line shape of the graphite-related systems (i.e., GICs, m-SWNTs, and monolayer graphene) that arise due to the presence of a Dirac cone or a linear energy band structure.

The BWF line shape is defined by the following formula:

$$I_{\mathrm{BWF}}(\omega_s) = I_0 \frac{(1 + s/q_{\mathrm{BWF}})^2}{1 + s^2}$$
$$= I_0 \left[\frac{1}{q_{\mathrm{BWF}}^2} + \frac{1 - 1/q_{\mathrm{BWF}}^2}{1 + s^2} + \frac{2s/q_{\mathrm{BWF}}}{1 + s^2} \right], \quad (1)$$

where $s = (\omega_s - \omega_G)/\Gamma$. Here ω_s, ω_G, $1/q_{\mathrm{BWF}}$, Γ, and I_0 are the Raman shift, the spectral peak position, the asymmetric factor, the spectral width, and the maximum intensity of the BWF spectra, respectively. The right-hand side of Eq. (1) tells us that the BWF line shape, respectively, consists of a constant continuum spectrum, a discrete Lorentzian spectrum, and an interference effect between both spectra. When $1/q_{\mathrm{BWF}} = 0$, Eq. (1) gives a Lorentzian line shape which represents a discrete phonon spectrum. The interference term gives rise to an asymmetric line shape for positive and negative values of s, in which the asymmetry is proportional to a dimensionless parameter $1/q_{\mathrm{BWF}}$, mimicking the ratio between the probability amplitude of the continuum spectra to that of

the discrete spectra [8]. In the Raman spectroscopy studies of graphite-related systems [10,11], the continuum spectra come from the electronic excitations and are usually observed only in metallic systems. The BWF line shapes in graphene have been found in various kinds of phenomena such as scanning tunneling microscopy [12], optical conductivity [13], photoabsorption spectroscopy [14], and infrared spectroscopy [15,16], revealing that electron-hole pair excitations in the vicinity of the Dirac cone play an important role in the continuum spectra.

The asymmetric BWF line shapes in graphite-related systems are normally found in the Raman shift around 1600 cm^{-1}, known as the *G* modes, which correspond to two zone-center ($\mathbf{q} = 0$) phonon modes, namely the in-plane tangential optic (iTO) and longitudinal optic (LO) modes. In graphene, the BWF asymmetry of the *G* band is observed using gate-modulated Raman spectroscopy [9]. The asymmetric factor ($1/q_{\mathrm{BWF}}$) has a value around -0.06 or one-order of magnitude smaller than those found in m-SWNTs ($1/q_{\mathrm{BWF}} \approx -0.4$) [7] and in GICs ($1/q_{\mathrm{BWF}} \approx -0.5$) [6]. The absolute value of the BWF asymmetric factor greatly decreases as we change the Fermi energy (E_F) to be further from the Dirac point by applying a positive or a negative bias with respect to the charge neutrality point [9,17]. These results give a clue that the asymmetric factor strongly depends on the electronic density of states (DOS) near the Dirac cone.

In this work, we show that the origin of the BWF spectra in graphene comes from the continuous single-particle electron-hole pair spectra, interfering with the discrete phonon spectra. Hereafter, we refer to the single-particle electron-hole pair spectra as the electronic Raman scattering (ERS) spectra [18]. In the previous work for m-SWNTs, we discuss that the ERS spectra originate from the second-order Coulomb interaction with nonzero momentum transfer $\mathbf{q} \neq 0$, due to the symmetry of the A and B sublattice wave functions which gives rise to the absence of the direct Coulomb interaction at the zone center $\mathbf{q} = 0$ [19]. Unlike the previous calculation for m-SWNTs which utilized exciton wave functions [19], in this calculation we use electron wave functions from the tight-binding (TB) approximation because our calculation regime (2.4 eV) is far from the saddle-point energy dispersion (4 eV), and thus the exciton effects are negligible [14,20]. The use of electron wave functions gives considerable contributions of the intervalley

---

*hasdeo@flex.phys.tohoku.ac.jp

scattering to the Raman intensity which was neglected in the previous study [19]. After calculating the Raman amplitudes of the ERS and the phonon spectra, we found that the interference between the ERS and the phonon spectra gives a drastic change in the constructive-destructive interference near the phonon spectra, giving an asymmetry to the phonon line shape when fitted to the BWF line shape. By considering the second-order Raman process, we systematically reproduce the E_F dependence of the Raman spectra of graphene that was observed in the experiment [9].

This paper is organized as follows. In Sec. II we describe our calculation method for the electron-electron interaction using the TB approximation and considering up to second-order Raman processes. In Sec. III, we discuss the calculated ERS spectra as a function of E_F, and we compare the asymmetric BWF factor $1/q_{\mathrm{BWF}}$ obtained from our calculation with that from experiment. Finally, in Sec. IV we give a summary of this work.

II. THEORETICAL METHODS

The possible Raman scattering processes considered in this calculation are the G Raman scattering [Fig. 1(a)] and the ERS [Figs. 1(b)–1(f)]. The ERS consists of either intravalley (A) or intervalley (E) interaction, either intravalley (a) or intervalley (e) scattering, and either zero momentum transfer ($\mathbf{q} = 0$ first-order) or nonzero momentum transfer ($\mathbf{q} \neq 0$ second-order) processes [19]. When a photon with the laser excitation energy E_L is introduced to the graphene sample, the photon excites an electron from an initial state i to an intermediate state n with an energy matched to E_L (incident resonance) with an uncertainty $\gamma = 0.1$ eV due to the finite lifetime of the electron-photon interaction.

We realized that there is also a contribution of the nonresonant Raman process to the G-band intensity [21]. In

Appendix A, we show that the resonant Raman calculation with an uncertainty $\gamma = 0.1$eV produces the G-band peak intensity with the same magnitude compared with that of the full Brillouin-zone calculation including nonresonant terms. Although the nonresonant terms cannot be neglected in the real case, the presence of the nonresonant term will not change the origin of the BWF asymmetry discussed in this paper. Therefore we simply neglect the nonresonant terms for reducing the necessary computational time.

The photoexcited electron (PE) is then scattered to another intermediate state n' either by the electron-phonon interaction (phonon Raman scattering) or by the Coulomb interaction (ERS) which excites the Dirac electrons (DEs) on the Dirac cone and the electron finally recombines with a hole by emitting a scattered photon energy E_S as shown in Fig. 1. Both the phonon Raman scattering and ERS processes share the same initial and final states. In the ERS, the Coulomb interaction between the PE and the DEs causes the PE to reduce its energy and changes the PE's momentum while the DEs are being excited. We neglect the photon-assisted ERS process without the Coulomb interaction (zeroth-order ERS), reported by Kashuba and Fal'ko [22], because we found that these spectra do not coexist with the G band at $|E_F| > \omega_G/2$ and that these spectra originate from nonresonant phenomena. Our detailed analysis to neglect the zeroth-order ERS is presented in Appendix B.

The number of DEs to be excited for each process depends on the number of the scattering order. In the first-order process, only one DE is excited and this process requires a zero momentum transfer ($\mathbf{q} = 0$) since the PE momentum ($\mathbf{k}$) should be the same as its hole momentum in order to emit a scattered photon with energy E_S by the electron-hole recombination process. In the second-order process, on the other hand, the PE is scattered twice ($\mathbf{k} \rightarrow \mathbf{k} - \mathbf{q}$) and ($\mathbf{k} - \mathbf{q} \rightarrow \mathbf{k}$) and the PE excites two DEs with relative nonzero
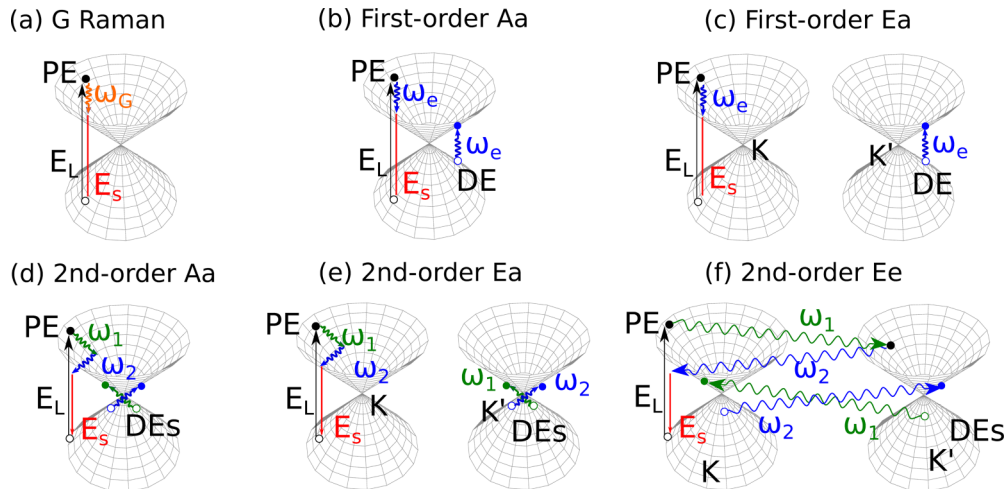

FIG. 1. (Color online) All possible Raman scattering processes considered in Eq. (2): (a) the G Raman scattering with the Raman shift $\omega_s = \omega_G$, (b)–(f) the electronic Raman scattering (ERS) processes. The ERS processes include the Coulomb interactions between a photoexcited electron (PE) and electrons on the Dirac cone (DEs): (b) a first-order intravalley interaction and intravalley scattering (Aa), (c) a first-order intervalley interaction and intravalley scattering (Ea), (d) a second-order intravalley interaction and intravalley scattering (Aa), (e) a second-order intervalley interaction and intravalley scattering (Ea), and (f) a second-order intervalley interaction and intervalley scattering (Ee). Capital (small) letters A (a) and E (e) label the intravalley and the intervalley interactions (scatterings). Here E_L and E_S are the laser excitation energy and scattered photon energy, respectively. The Raman shift for the first- (second-) order processes is $\omega_s = \omega_e(\omega_s = \omega_1 + \omega_2)$.

electron-hole momenta $-\mathbf{q}$ and $\mathbf{q}$. Due to the degeneracy of the Dirac cone at the K and K' points of the graphene Brillouin zone (BZ), both the first-order processes and the second-order processes may occur either in the intravalley (A) interactions or in the intervalley (E) interactions.

In the A interactions, the DEs are excited on the same Dirac cone as the PE, while in the E interactions, the DEs are excited on the other Dirac cone. In the case of the E interaction, the initial and final states of the PE and DEs can be in the same (different) valley which is defined by intravalley (intervalley) scattering labeled by a small letter "a" ("e"). The e scattering is not possible in the A interaction because the $+\mathbf{q}$ and $-\mathbf{q}$ scattering are pointing to two different directions at the high-symmetry points of graphene; one is pointing to the $\overline{KK'}$ direction while the other is pointing to the $\overline{K\Gamma}$ direction. Thus the Ae interaction does not conserve energy during the scattering processes. Combining all possible A and E interactions with the a and e scatterings, we have an Aa [Fig. 1(b)] and an Ea [Fig. 1(c)] in the first-order processes; and an Aa [Fig. 1(d)], an Ea [Fig. 1(e)], and an Ee [Fig. 1(f)] in the second-order processes.

The BWF asymmetry comes from the interference effect between the phonon spectra with the ERS because both spectra have the same initial and final states for a single PE (Fig. 1). Thus in order to calculate the Raman intensity, we first sum up all possible scattering amplitudes for given initial and final states, and then we take the square of the sum of amplitudes [10,23]

$$I(\omega_s) = [A_G(\omega_s) + A_{\mathrm{ERS}}(\omega_s)]^2, \qquad (2)$$

where $A_G = \sum_\nu A_\nu$, in which A_ν and A_{ERS} are, respectively, the νth phonon Raman scattering amplitude and the ERS scattering amplitude. The phonon Raman scattering amplitude is given by [24]

$$
\begin{aligned}
A_\nu(\omega_s) = \frac{1}{\pi} \sum_{n,n'} \Bigg[& \frac{\mathcal{M}_{\mathrm{el-op}}^{n,i}}{[\Delta E_{ni} - i\gamma]} \frac{\mathcal{M}_{\mathrm{el-}\nu}^{n',n}}{[\Delta E_{n'i} - \hbar\omega_G - i(\gamma + \Gamma_\nu)]} \\
& \times \frac{\mathcal{M}_{\mathrm{el-op}}^{f,n'}}{[E_L - \hbar\omega_G - \hbar\omega_s - i\Gamma_\nu]} \Bigg],
\end{aligned}
\qquad (3)
$$

where for the phonon modes we only consider the first-order process $\nu = $ iTO or LO modes, and $\Delta E_{ni} = E_L - E_n - E_i$. Here we use a broadening factor $\gamma = 0.1$ eV, which is related to the inverse of the lifetime of the photoexcited carriers. On the other hand, Γ_ν is related to the lifetime of the electron-phonon interaction [25].

The values of Γ_ν and ω_G are considered as follows. In the gate-modulated Raman spectra, we expect phonon frequency softening and spectral broadening as we shift the Fermi energy from $|E_F| > 0$ to $E_F = 0$. This effect is due to the Kohn anomaly, i.e., renormalization of the phonon energy by electron-hole pair excitation in the G-mode Raman spectra of graphene [4]. Since the Kohn anomaly is not a perturbation of the PE but rather a perturbation of the phonon, we do not consider the Kohn anomaly effect explicitly in this calculation, but we can fit the peak position $\omega_G = 1591 + 15|E_F|$ cm^{-1} for $-0.20 \leqslant E_F \leqslant 0.00$ eV and $\omega_G = 1591 + 22.5|E_F|$ cm^{-1} for $0.00 < E_F \leqslant 0.40$ eV. The inverse of the phonon lifetime is also fitted by $\Gamma_\nu = 5 - 10|E_F|$ cm^{-1} for $-0.20 \leqslant E_F$

< 0.25 eV and $\Gamma_\nu = 2.5$ cm^{-1} for $0.25 \leqslant E_F \leqslant 0.40$ eV so as to reproduce the experimental results [9]. It is important to note that the Kohn anomaly does not give an asymmetric BWF line shape of the G-band spectra because the Kohn anomaly is not an interference phenomenon; only the interference effect between the G band and the ERS does however show a BWF line shape. The electron-photon ($\mathcal{M}_{\mathrm{el-op}}^{b,a}$) and electron-phonon ($\mathcal{M}_{\mathrm{el-}\nu}^{b,a}$) matrix elements for a transition between states $a \to b$ are adopted from previous works within the TB method [26,27]. We approximate the intermediate states (virtual states) to become a real state with $n = n'$, which is a good approximation for the resonance condition [28].

The ERS amplitude A_{ERS} is the summation of the amplitude from the first-order $A_{\mathrm{ERS}}^{(1)}$ and second-order $A_{\mathrm{ERS}}^{(2)}$ processes. The amplitude of the first-order ERS process is given by

$$
\begin{aligned}
A_{\mathrm{ERS}}^{(1)}(\omega_s) = \frac{1}{\pi} \sum_{n,n'} \sum_{l,l'} \Bigg[& \frac{\mathcal{M}_{\mathrm{el-op}}^{n,i}}{[\Delta E_{ni} - i\gamma]} \\
& \times \frac{K_{n',l',n,l}(0)}{[\Delta E_{n'i} - \hbar\omega_e - i(\gamma + \Gamma_e)]} \\
& \times \frac{\mathcal{M}_{\mathrm{el-op}}^{f,n'}}{[E_L - \hbar\omega_e - \hbar\omega_s - i\Gamma_e]} \Bigg],
\end{aligned}
\qquad (4)
$$

where ω_e and $\Gamma_e = 30$ meV are, respectively, the energy of the excited DE electron and the inverse lifetime of the electron-electron interaction. The electron-electron interaction $K_{1,2,3,4}(\mathbf{q})$ defines the scattering of the PE [DE] from an initial state (1) [(2)] to a final state (3) [(4)] which consists of direct (K^d) and exchange (K^x) interaction terms,

$$K_{1,2,3,4}(\mathbf{q}) = K_{1,2,3,4}^d(\mathbf{q}) + K_{1,2,3,4}^x(\mathbf{q}), \qquad (5)$$

for a spin singlet state. We do not consider spin triplet states for simplicity due to the fact that the exchange interaction is sufficiently small [19,28]. The direct $K_{1,2,3,4}^d(\mathbf{q})$ and exchange $K_{1,2,3,4}^x(\mathbf{q})$ Coulomb interactions between two electrons in the TB approximation are given by

$$K_{1,2,3,4}^d(\mathbf{q}) = \sum_{ss'=\mathrm{A,B}} C_s^1 C_{s'}^2 C_s^{*3} C_{s'}^{*4} \mathrm{Re}\left[v_{ss'}(\mathbf{q})\right], \qquad (6)$$

$$K_{1,2,3,4}^x(\mathbf{q}) = \sum_{ss'=\mathrm{A,B}} C_s^1 C_{s'}^2 C_{s'}^{*3} C_s^{*4} \mathrm{Re}\left[v_{ss'}(\mathbf{k'} - \mathbf{k} - \mathbf{q})\right], \qquad (7)$$

where $[1,2,3,4] = [\mathbf{k}c, \mathbf{k'}v, (\mathbf{k}-\mathbf{q})c, (\mathbf{k'}+\mathbf{q})c]$ in the case of ERS in undoped graphene ($E_F = 0$) [Fig. 2(a)]. In the electron-doped ($E_F > 0$) and the hole-doped ($E_F < 0$) cases, we add possible intraband transitions $[2,4] = [\mathbf{k'}c, (\mathbf{k'}+\mathbf{q})c]$ and $[2,4] = [\mathbf{k'}v, (\mathbf{k'}+\mathbf{q})v]$, respectively, as long as state (2) is occupied and state (4) is unoccupied. C_s^j is a tight-binding coefficient for an atomic site $s = $ A, B and a state j [29]. The Fourier transform of the Coulomb potential $v_{ss'}(\mathbf{q})$ is defined by

$$v_{ss'}(\mathbf{q}) = \frac{1}{N} \sum_{u'} e^{i\mathbf{q}\cdot(\mathbf{R}_{u's'} - \mathbf{R}_{0s})} v(\mathbf{R}_{0s}, \mathbf{R}_{u's'}), \qquad (8)$$
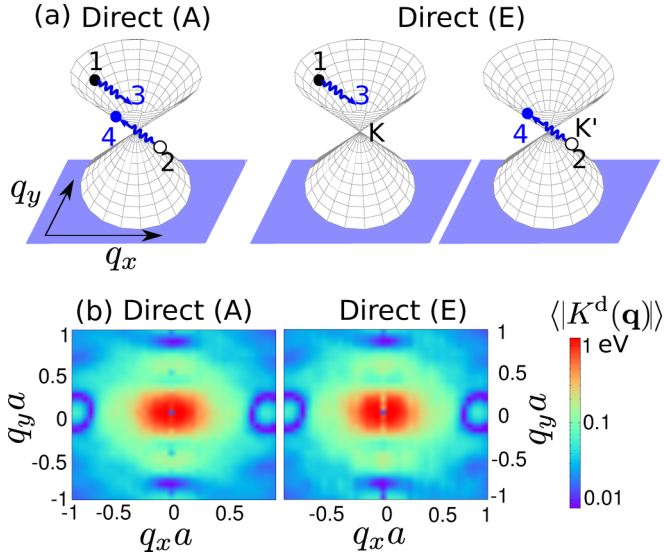
FIG. 2. (Color online) (a) Illustration of the direct Coulomb intravalley (A) interaction and intervalley (E) interaction involving states around K and K' Dirac cones. (b) The averaged absolute value of the direct Coulomb interaction matrix element K^{d} as a function of momentum transfer $\mathbf{q}$ for the intravalley (A) interaction and for the intervalley (E) interaction. The intervalley scattering is not shown in this figure.

where $v(\mathbf{R},\mathbf{R}')$ is the effective Coulomb potential for the π electron system modeled by the Ohno potential [28,30]

$$v(\mathbf{R},\mathbf{R}') = \frac{U_0}{\sqrt{\left(\frac{4\pi\epsilon_0}{e^2} U_0 \, |\mathbf{R} - \mathbf{R}'|\right)^2 + 1}}, \qquad (9)$$

in which U_0 is the on-site Coulomb potential for two π electrons at the same site $\mathbf{R} = \mathbf{R}'$, defined by

$$U_0 = \int d\mathbf{r} d\mathbf{r}' \frac{e^2}{|\mathbf{r} - \mathbf{r}'|} \phi_\pi^2(\mathbf{r})\phi_\pi^2(\mathbf{r}') = 11.3 \text{ eV}. \qquad (10)$$

The amplitude of the second-order ERS process is given by

$$
\begin{aligned}
A_{\mathrm{ERS}}^{(2)}(\omega_{\mathrm{s}}) = \frac{1}{\pi} \sum_{n,n',n''} \sum_{m,m',l,l'} &\left[\frac{\mathcal{M}_{\mathrm{el-op}}^{n,i}}{[\Delta E_{ni} - i\gamma]} \right. \\
&\times \frac{K_{n',m',n,m}^{\mathrm{d}}(\mathbf{q})}{[\Delta E_{n'i} - \hbar\omega_1 - i(\gamma + \Gamma_{\mathrm{e}})]} \\
&\times \frac{K_{n'',l',n',l}^{\mathrm{d}}(-\mathbf{q})}{[\Delta E_{n''i} - \hbar\omega_1 - \hbar\omega_2 - i(\gamma + 2\Gamma_{\mathrm{e}})]} \\
&\times \left. \frac{\mathcal{M}_{\mathrm{el-op}}^{f,n'}}{[E_{\mathrm{L}} - \hbar\omega_1 - \hbar\omega_2 - \hbar\omega_{\mathrm{s}} - 2i\Gamma_{\mathrm{e}}]} \right], \qquad (11)
\end{aligned}
$$

where we also consider the same virtual state approximation as in Eq. (3). Here, ω_1 and ω_2 are the energies of the DEs emitted for the electron-electron interaction in the second-order ERS process.

III. ELECTRONIC RAMAN SPECTRA AND THE BWF ASYMMETRY

Since the electron-electron interaction depends on initial states (1,2) of PE and DE and also on a momentum transfer ($\mathbf{q}$), we consider the absolute average value of the matrix elements over the initial states in order to visualize the strength of the electron-electron interaction in a simple manner. The direct Coulomb interaction can occur in either the A or E interaction as shown in Fig. 2(a). Figure 2(b) depicts the absolute average value of $K_{1,2,3,4}^{\mathrm{d}}(\mathbf{q})$ over the initial states (1,2)

$$\langle |K_\mu^{\mathrm{d}}(\mathbf{q})| \rangle = \frac{1}{N_1 N_2} \sum_{(1,2)} |K_{1,2,3,4}^{\mathrm{d}}(\mathbf{q})|, \qquad (12)$$

where $\mu = $ A and E. The e (intervalley) scattering is not shown in Fig. 2(b) for a convenient comparison between the A and E interactions, since the A interaction does not have the e scattering. $\langle |K_\mu^{\mathrm{d}}(\mathbf{q})| \rangle$ only depends on $\mathbf{q}$ after taking the summation over the initial states (1,2) because the final states (3,4) depend on (1,2) by momentum conservation in Eq. (6). As shown in Fig. 2(b), for both the A and E interactions, K^{d} disappears at $\mathbf{q} = 0$, indicated by a small black dot at $\mathbf{q} = (0,0)$, due to the symmetry of the A and B sublattice wave functions in the graphene unit cell which cancel in the summation of K^{d} in Eq. (6) [19]. The absence of a direct Coulomb interaction suggests that the ERS should come from the second-order $\mathbf{q} \neq 0$ electron-electron interaction, similar to what we found in m-SWNTs [19]. The first-order ERS can only be possible by means of the exchange Coulomb interaction. Although we take into account the exchange Coulomb interaction, the Raman intensity from the first-order process is still six orders of magnitude smaller than that of the second-order process [see inset of Fig. 3(a)]. Therefore, we can neglect the first-order processes for both the A and E interactions.

In Fig. 3 we present results for the Raman intensity calculation $I(\omega_{\mathrm{s}})$ of Eq. (2). The solid black curve in Fig. 3(a) shows the total Raman intensity after considering the interference of the G-mode spectra with the ERS spectra, while the dashed red line shows the Lorentzian G phonon spectra by taking the square of its probability amplitudes $A_G(\omega_{\mathrm{s}})$ [Eq. (3)]. The G-mode constituents, i.e., the iTO and LO modes, are indicated by a blue dotted line and a blue dot-dashed line, respectively. It is clear from Fig. 3(a) that the calculated Raman spectra show asymmetry around the peak position at 1590 cm^{-1}. By fitting the calculated result to Eq. (1), we obtain the fitted values of $1/q_{\mathrm{BWF}}$, which have the same negative sign as the experimental data [9]. For a negative $1/q_{\mathrm{BWF}}$, when ω_{s} is smaller (greater) than ω_G, $I(\omega_{\mathrm{s}})$ is greater (smaller) than $|A_G(\omega_{\mathrm{s}})|^2$, indicating that the interference between the G mode and the ERS spectra is constructive (destructive) below (above) the resonance condition $\omega_{\mathrm{s}} = \omega_G$.

By decreasing (increasing) E_F further from the Dirac cone, transitions from (to) the unoccupied (occupied) states are suppressed due to the Pauli principle. Thus we expect that the asymmetric factor $1/q_{\mathrm{BWF}}$ decreases as we change the E_F from the Dirac point $E_F = 0.00$ eV to $E_F = 0.20$ eV as shown in Fig. 3(b). The solid black line is the intensity of the spectrum with $1/q_{\mathrm{BWF}} = -0.073$ when $E_F = 0.00$ eV, while the blue
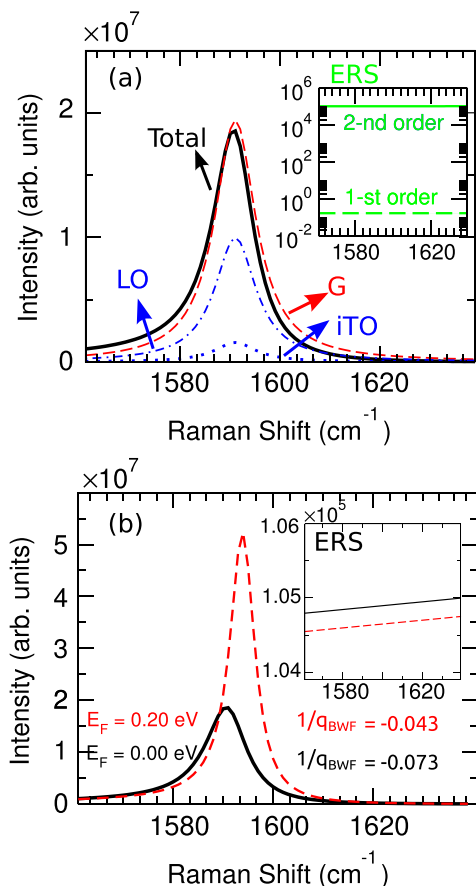
FIG. 3. (Color online) (a) Calculated Raman intensity according to Eq. (2) for $E_F = 0.00$ eV (solid line) compared with the Lorentzian G mode intensity by taking the square of A_G in Eq. (3) (dashed line). The G-mode constituents, i.e., iTO and LO, are indicated by a dotted line and a dot-dashed line, respectively. An asymmetric line shape (solid line) appears due to the interference effect between the G mode with the ERS. The inset shows calculated results of the first-order (dashed line) and the second-order (solid line) ERS spectra, indicating that the second-order processes have an intensity value six orders of magnitude greater than that of the first-order processes. (b) Calculated Raman intensity for $E_F = 0.00$ eV (solid line) and $E_F = 0.20$ eV (dashed line). The BWF asymmetric factor $1/q_{\text{BWF}}$ decreases by increasing the absolute value of $|E_F|$ away from the Dirac point because the ERS intensity also decreases by increasing $|E_F|$ (inset).

dashed line is the corresponding curve with $1/q_{\text{BWF}} = -0.043$ when $E_F = 0.20$ eV. The Raman intensity and peak position at $E_F = 0.20$ eV are larger than that at $E_F = 0.00$ eV due to the Kohn anomaly effect [4].

Unlike the ERS spectra in m-SWNTs which are Lorentzian functions [18,19], the ERS intensity in graphene is a linear function of ω_s [inset of Fig. 3(b)]. The positive gradient of the ERS intensity is due to the greater scattering path available to excite DEs in the second-order processes as ω_s increases. The ERS intensity will increase monotonically and will get saturated at $\omega_s \geq E_L/2$. The absence of the ERS peak intensity in graphene is related to the absence of Van Hove singularities within the G-mode energy ~ 0.2 eV to $E_L = 2.4$ eV. The absence of the ERS peak also becomes the reason why the

$1/q_{\text{BWF}}$ values of the G mode in graphene are one order of magnitude smaller compared to those in m-SWNTs. The ERS intensity is about two orders of magnitude smaller than that of the G mode, and by increasing the E_F the ERS intensity decreases only less than 1%; nevertheless the change of the $1/q_{\text{BWF}}$ is significant [Fig. 3(b)]. Thus, this BWF feature is very sensitive to the presence or absence of the continuum spectra.

In Figs. 4(a) and 4(b), we respectively show our calculated result and the corresponding experimental results (Ref. [9]) for the G-band Raman intensity as a function of the Raman shift, which is plotted for various values of E_F in the range $-0.20 \leq E_F \leq 0.40$ eV. In the original version [9], Fig. 4(b) was given as a function of gate voltages V_G. For our present purpose of comparing the calculated results and experimental results, we here convert V_G to E_F using the relation $E_F = \text{sgn}(V_G - V_0)\hbar v_F \sqrt{\alpha\pi|V_G - V_0|}$ where the Fermi velocity $v_F = 10^8$ cm/s, the constant voltage adjusted to the Dirac point $V_0 = -57.5$ V, and the capacitance $\alpha = 7.2 \times 10^{10}$ cm^{-2} V^{-1} for the SiO$_2$ dielectric medium with a thickness 300 nm [9,17,31]. At the charge neutrality point $E_F = 0.00$ eV, the G-band spectrum is broadened and its frequency is softened due to the Kohn anomaly effect.

Comparison of the BWF asymmetric factor $1/q_{\text{BWF}}$ between the theory (square) and experiment (circle) shows a reasonable agreement, as can be seen in Fig. 4(c), except for $E_F \geq 0.20$ eV where the experimental results deviate from the calculated results. We suppose that the deviation is related to the difficulties of observing the BWF asymmetry at $E_F > 0.20$ eV in the experiment because the continuum ERS intensity is about two or three orders of magnitude smaller compared to the G-band intensity. Such weak ERS spectra might couple strongly with the background spectra in the experiment which makes the ERS contribution difficult to observe. The calculated asymmetric factor $1/q_{\text{BWF}}$ has a V-shaped curve structure as a function of E_F with the dip position at $E_F = 0.00$ eV. The decrease of $1/q_{\text{BWF}}$ is related to the decrease of the ERS intensity due to the suppression of electron-hole pair excitations on the Dirac cone upon doping.

The present agreement between experiment and the theory also reconfirms that plasmons do not contribute to the continuum spectra. The physical reason is as follows. When $|E_F| > 0$, collective excitations (plasmons) are expected to be generated, and consequently the ERS spectra should be enhanced [32]. However, what we obtain in the present study is that the ERS spectra are in fact suppressed if we increase $|E_F|$. Therefore, we rule out the contribution of plasmons in the ERS spectra and we conclude that only single-particle electron-hole pair excitations are important.

IV. SUMMARY

We have shown that the origin of the BWF spectra in graphene comes from the continuum single-particle electron-hole pair ERS spectra interfering with the discrete G-band phonon spectra. By calculating the Raman amplitudes of the ERS and the phonon spectra, we found that the interference effect between the ERS and the phonon spectra gives a drastic change in the constructive-destructive interference near the phonon resonance condition, leading to an asymmetry of
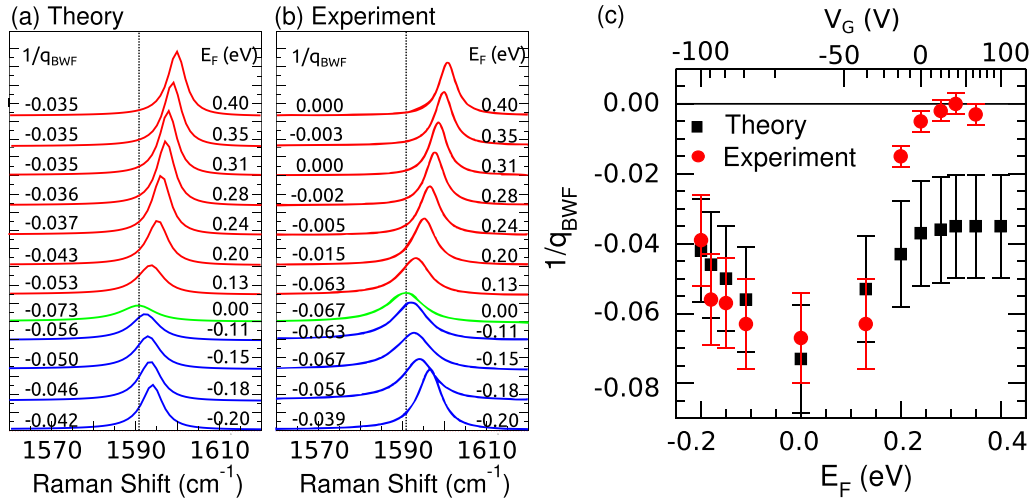
FIG. 4. (Color online) Comparison between (a) the calculated results (this work) and (b) the experimental results taken from Ref. [9] for the G-band Raman intensity as a function of the Raman shift, which is plotted for various values of E_F in the range $-0.20 \leqslant E_F \leqslant 0.40$ eV. The values of $1/q_{BWF}$ obtained from the calculation and the experiment are also given on each plot. (c) Comparison of the BWF asymmetric factor $1/q_{BWF}$ as a function of E_F and gate voltage V_G between theory (squares) and experiment (circles). Both the linewidth and the phonon peak frequency shift due to the Kohn anomaly effect are fitted from the experimental results in Ref. [9].

the phonon line shape when fitted to the BWF line shape. Considering the second-order Raman process, we are able to reproduce the E_F dependence of the Raman spectra systematically. We expect that the asymmetric BWF feature appears generally in the phonon Raman spectra of all Dirac cone systems.

APPENDIX A: ROLE OF NONRESONANT PROCESSES IN THE G-BAND INTENSITY

Unlike the density of states (DOS) of carbon nanotubes which possesses many Van Hove singularities due to the nature of one-dimensional systems, the graphene DOS is not singular when we excite graphene with E_L below the ultraviolet region $\sim$5 eV. Therefore, considering the nonresonant contributions to the G-band intensity is important [21]. In Fig. 5(a), we calculate the contribution of the electron initial states to the G-band Raman intensity. The light polarization is chosen to be parallel to the $\mathbf{k}_x$ direction, and we assumed that the light polarization direction does not affect the G-band intensity. We found that the dominant contribution comes from the resonance condition as shown by the trigonal-like shape of the energy bands surrounding K and K' points. From this plot, we can find the electron energy E dependence of the G-band intensity as plotted in Fig. 5(b).

The dominant contribution to the G-band intensity comes from the resonance effect when $E = E_L$ with FWHM = 0.2 eV. The nonresonant terms play a role when we consider the summation over all possible electron initial states in the Raman amplitude $A_G(\omega_s)$. Depending on the $A_G(\omega_s)$ phase, the interference between the initial states can be constructive or destructive. We plot the G-band phase at a Raman shift $\omega_s = 1560$ cm^{-1} in Fig. 5(c), where $\varphi(\omega_s) = \tan^{-1}[\text{Re}A_G(\omega_s)/\text{Im}A_G(\omega_s)]$. Phase shifts occur near the resonance condition which is what we expect for a Lorentzian function. Another factor influencing the phase shift is related to the change of the sign of the matrix elements at the border of curved lines connecting the Γ and K points [27].

The G-band peak intensity as a function of the cutoff energy E_{cut} is shown in Fig. 5(d). When we take the initial states in the Brillouin zone (BZ) which satisfy $\Delta E_{ni} \leqslant E_{cut}$ [Eq. (3)], 0.1 eV $\leqslant E_{cut} \leqslant \infty$, then we can see how the G-band peak intensity oscillates due to the interference effect of the initial states. In the paper, we consider only a resonance condition with $E_{cut} = \gamma = 0.1$ eV and it produces the G-band peak intensity with the same magnitude compared to that of $E_{cut} = \infty$ (when we consider the whole Brillouin zone). Although in the real case we cannot neglect the nonresonant terms, the origin of the BWF asymmetry does not change even if we take the resonant terms into account.

APPENDIX B: THE ZEROTH-ORDER ELECTRONIC RAMAN SPECTRA

In an earlier study of electronic Raman scattering in graphene, Kashuba and Fal'ko proposed that the electronic Raman scattering (ERS) processes without the Coulomb interaction, simply referred to as zeroth-order ERS, should contribute to the continuum spectra [22]. Although the zeroth-order ERS spectra exist, here we prove that their contributions to the total ERS spectra are negligible. One of the possible zeroth-order ERS processes is illustrated in Fig. 6(a). An
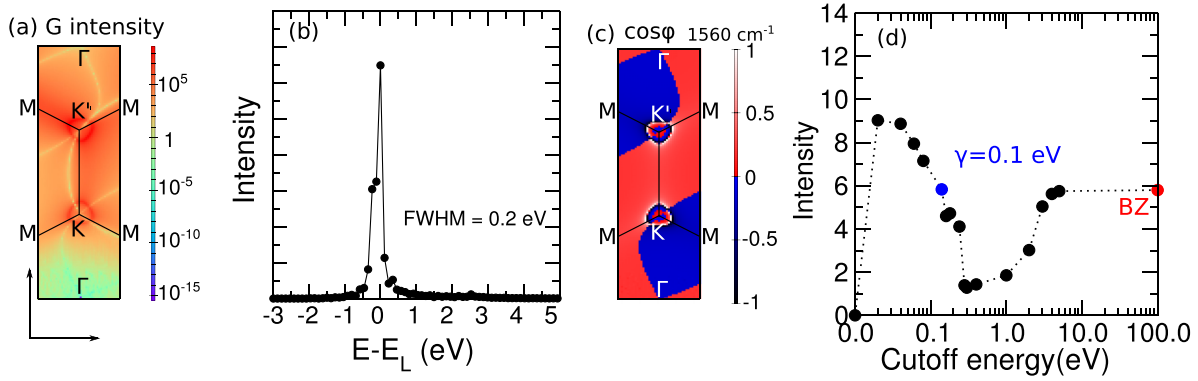
FIG. 5. (Color online) (a) The G-band intensity as a function of electron initial states in the first Brillouin zone, (b) the G-band intensity as a function of electron energy, (c) the G-band phase $\cos\varphi(\omega_s)$, where $\varphi(\omega_s) = \tan^{-1}[\text{Re}A_G(\omega_s)/\text{Im}A_g(\omega_s)]$, (d) the G-band peak intensity as a function of cutoff energy measured from E_L. In this plot we use $E_L = 2.4$ eV, $E_F = 0$ eV, and resonance window $\gamma = 0.1$ eV.

electron in an initial state $|i\rangle$ with energy ϵ_i and momentum $\mathbf{k}_i$ absorbs a photon with energy E_L. The electron is then excited to a virtual state $|n\rangle$ and scatters a photon with energy E_S and finally occupies a state $|f\rangle$ in the conduction band with energy $\epsilon_f = \epsilon_i + \hbar\omega_s$ and momentum $\mathbf{k}_i + \mathbf{q}$. In this case, ω_s and $\mathbf{q}$ are the Raman shift and momentum change due to electron-photon scattering, respectively. Another possible zeroth-order ERS process differs from Fig. 6(a) only by the sequence of the photon emission and absorption processes that are occurring. We expect that such a contribution has the same order of magnitude of intensity as that in Fig. 6(a). Therefore, we mainly focus on the contribution sketched in Fig. 6(a) to be compared with the ERS spectra considered in this paper.

To calculate the Raman intensity for the process shown in Fig. 6(a), we need to consider an approximation of a virtual state as an intermediate state. A virtual state $|n\rangle$ is defined as a linear combination of real states $|n\rangle = \sum_k B_k |k\rangle$, where $|k\rangle$ is the eigenstate of the unperturbed Hamiltonian (in this case, it is a tight-binding wave function) such that $H|k\rangle = \epsilon_k |k\rangle$. The information about the valence or conduction band has been assumed to be implied within $|k\rangle$. The coefficient B_k can be obtained from the time-dependent perturbation theory of the electron-photon interaction as follows [19]:

$$B_k = \frac{\sqrt{N_B} M_{\text{el-op}}^{ki}}{E_L - \epsilon_{ki} - i\gamma}, \qquad (B1)$$

where $M_{\text{el-op}}^{ki} = \langle k|H_{\text{el-op}}|i\rangle$ is the electron-photon matrix element responsible for the transition from a state i to a state k, N_B is a normalization constant, and γ is a broadening factor due to the finite lifetime of the electron-photon interaction. Here we set $\gamma = 0.1$ eV and we define $\epsilon_{ki} = \epsilon_k - \epsilon_i$. The Raman scattering amplitude A_0 of the process shown in Fig. 6(a) is given by the formula

$$A_0 = \sum_{i,n} \frac{M_{\text{el-op}}^{fn} M_{\text{el-op}}^{ni}}{E_L - \epsilon_{ni} - i\gamma} \delta(\mathbf{k}_i - \mathbf{k}_n)\delta(\mathbf{k}_n - \mathbf{k}_f)$$
$$\times \delta(E_L - \epsilon_{fi} - E_S), \qquad (B2)$$

with $M_{\text{el-op}}^{fn} = \langle f|H_{\text{el-op}}|n\rangle$, $M_{\text{el-op}}^{ni} = \langle n|H_{\text{el-op}}|i\rangle$, $\epsilon_{ni} = \epsilon_n - \epsilon_i$, and $\epsilon_{fi} = \epsilon_f - \epsilon_i = \hbar\omega_s$.

The first two delta functions appearing in Eq. (B2) are due to the momentum conservation and the third delta function is related to the energy conservation, where for simplicity we assume that only a vertical transition or $\mathbf{q} = 0$ process occurs. By the definition of the virtual states $|n\rangle$, we can simplify the Raman scattering amplitude as

$$A_0 = \sum_{i,k} B_k^2 \frac{M_{\text{el-op}}^{kk} M_{\text{el-op}}^{ki}}{E_L - \epsilon_{ki} - i\gamma} \delta(E_L - \epsilon_{ki} - E_S). \qquad (B3)$$

The calculated Raman intensity as a function of the Raman shift considering all processes is shown in Figs. 6(b) and 6(c)
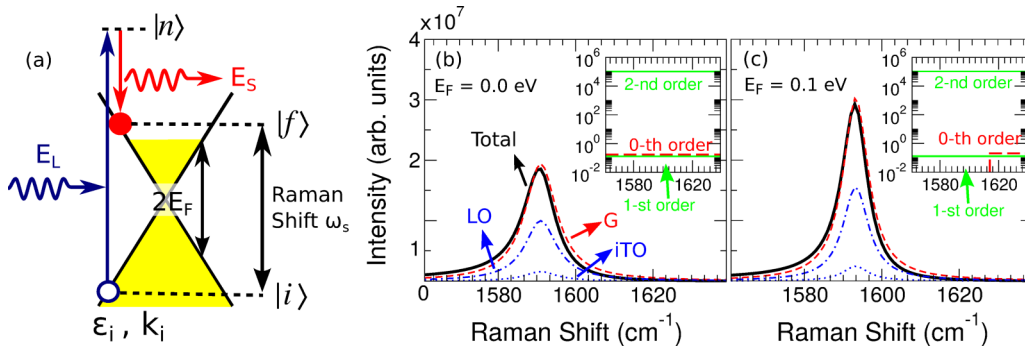

FIG. 6. (Color online) (a) Schematic of the zeroth-order ERS process, which is equivalent to the ERS Feynman diagram given by Kashuba and Fal'ko in Ref. [22]. Panels (b) and (c) show the calculated Raman intensity for $E_F = 0$ eV and $E_F = 0.1$ eV, respectively. Insets show contribution from the zeroth-, first-, and second-order ERS processes to the Raman intensity.

for $E_F = 0$ eV and $E_F = 0.1$ eV, respectively. We can see in Fig. 6(c) that the intensity of the zeroth-order ERS starts from a Raman shift $2|E_F| = 0.2$ eV ~ 1600 cm^{-1}.

There are two reasons why we can safely neglect the zeroth-order ERS in the calculation of the Raman intensity discussed in the main text. First, E_F in the experiment of Ref. [9] is changed from -0.2 to 0.4 eV, which is four times the energy of $\omega_G/2 = 0.1$ eV. If we suppose that the zeroth-order ERS is responsible for the origin of the BWF line shapes, we would expect that the asymmetry factor would go to zero for $E_F > \omega_G/2 = 0.1$ eV. However, the experiment shows that even at $E_F = 0.2$ eV the *G*-band asymmetry (BWF line shapes) can be seen, which indicates that the zeroth-order ERS process is not the origin of the asymmetry. Second, we can see that the zeroth-order ERS intensity is less than the second-order ERS considered in this paper by 6 orders of magnitude. The zeroth-order ERS intensity is also just on the same order of magnitude as the first-order ERS. Such small intensity values of the zeroth-order ERS come from the nonresonant processes. On the other hand, we obtained much larger values for the second-order ERS intensity because the process is doubly resonant. Therefore, we conclude that the zeroth-order ERS processes do not significantly contribute to the BWF asymmetry.

[1] L. M. Malard, J. Nilsson, D. C. Elias, J. C. Brant, F. Plentz, E. S. Alves, A. H. Castro Neto, and M. A. Pimenta, Phys. Rev. B **76**, 201401 (2007).

[2] D. L. Mafra, G. Samsonidze, L. M. Malard, D. C. Elias, J. C. Brant, F. Plentz, E. S. Alves, and M. A. Pimenta, Phys. Rev. B **76**, 233407 (2007).

[3] M. Lazzeri, S. Piscanec, F. Mauri, A. C. Ferrari, and J. Robertson, Phys. Rev. B **73**, 155426 (2006).

[4] S. Piscanec, M. Lazzeri, F. Mauri, A. C. Ferrari, and J. Robertson, Phys. Rev. Lett. **93**, 185503 (2004).

[5] M. S. Dresselhaus, A. Jorio, and R. Saito, Annu. Rev. Condens. Matter Phys. **1**, 89 (2010).

[6] P. C. Eklund and K. R. Subbaswamy, Phys. Rev. B **20**, 5157 (1979).

[7] S. D. M. Brown, A. Jorio, P. Corio, M. S. Dresselhaus, G. Dresselhaus, R. Saito, and K. Kneipp, Phys. Rev. B **63**, 155414 (2001).

[8] U. Fano, Phys. Rev. **124**, 1866 (1961).

[9] D. Yoon, D. Jeong, H. Lee, R. Saito, Y. Son, H. Lee, and H. Cheong, Carbon **61**, 373 (2013).

[10] A. Jorio, M. S. Dresselhaus, R. Saito, and G. Dresselhaus, *Raman Spectroscopy in Graphene-Related Systems* (Wiley, 2011).

[11] R. Saito, M. Hofmann, G. Dresselhaus, A. Jorio, and M. S. Dresselhaus, Adv. Phys. **60**, 413 (2011).

[12] T. O. Wehling, H. P. Dahal, A. I. Lichtenstein, M. I. Katsnelson, H. C. Manoharan, and A. V. Balatsky, Phys. Rev. B **81**, 085413 (2010).

[13] K. F. Mak, J. Shan, and T. F. Heinz, Phys. Rev. Lett. **106**, 046401 (2011).

[14] D. Chae, T. Utikal, S. Weisenburger, H. Giessen, K. v. Klitzing, M. Lippitz, and J. Smet, Nano Lett. **11**, 1379 (2011).

[15] A. B. Kuzmenko, I. Crassee, D. van der Marel, P. Blake, and K. S. Novoselov, Phys. Rev. B **80**, 165406 (2009).

[16] T. Tang, Y. Zhang, C. Park, B. Geng, C. Girit, Z. Hao, M. C. Martin, A. Zettl, M. F. Crommie, S. G. Louie, Y. R. Shen, and F. Wang, Nat. Nanotechnol. **5**, 32 (2010).

[17] R. Saito, K. Sato, P. T. Araujo, D. L. Mafra, and M. S. Dresselhaus, Solid State Commun. **175-176**, 18 (2013).

[18] H. Farhat, S. Berciaud, M. Kalbac, R. Saito, T. F. Heinz, M. S. Dresselhaus, and J. Kong, Phys. Rev. Lett. **107**, 157401 (2011).

[19] E. H. Hasdeo, A. R. T. Nugraha, K. Sato, M. S. Dresselhaus, and R. Saito, Phys. Rev. B **88**, 115107 (2013).

[20] L. Yang, J. Deslippe, C.-H. Park, M. L. Cohen, and S. G. Louie, Phys. Rev. Lett. **103**, 186802 (2009).

[21] D. Basko, New J. Phys. **11**, 095011 (2009).

[22] O. Kashuba and V. I. Fal'ko, Phys. Rev. B **80**, 241404 (2009).

[23] J. Friedman and R. Hochstrasser, Chem. Phys. Lett. **32**, 414 (1975).

[24] P. Y. Yu and M. Cardona, *Fundamentals of Semiconductors: Physics and Materials Properties* (Springer, Berlin, 2010).

[25] K. Sato, R. Saito, A. R. T. Nugraha, and S. Maruyama, Chem. Phys. Lett. **497**, 94 (2010).

[26] J. Jiang, R. Saito, Ge. G. Samsonidze, S. G. Chou, A. Jorio, G. Dresselhaus, and M. S. Dresselhaus, Phys. Rev. B **72**, 235408 (2005).

[27] A. Grüneis, R. Saito, Ge. G. Samsonidze, T. Kimura, M. A. Pimenta, A. Jorio, A. G. Souza Filho, G. Dresselhaus, and M. S. Dresselhaus, Phys. Rev. B **67**, 165402 (2003).

[28] J. Jiang, R. Saito, Ge. G. Samsonidze, A. Jorio, S. G. Chou, G. Dresselhaus, and M. S. Dresselhaus, Phys. Rev. B **75**, 035407 (2007).

[29] K. Sasaki and R. Saito, Prog. Theor. Phys. **176**, 253 (2008).

[30] V. Perebeinos, J. Tersoff, and P. Avouris, Phys. Rev. Lett. **92**, 257402 (2004).

[31] K. S. Novoselov, A. K. Geim, S. V. Morozov, D. Jiang, M. I. Katsnelson, I. V. Grigorieva, S. V. Dubonos, and A. A. Firsov, Science **306**, 666 (2004).

[32] E. H. Hwang and S. Das Sarma, Phys. Rev. B **75**, 205418 (2007).